Composite superlattice radio-frequency surface-acoustic-wave devices

Farrukh Najmi,[1,2,*] Howard Yawit,[1,2] Wataru Takeda,[1,2] Abhirup Basu,[1,2] Samarjith Biswas,[1,2] Zafer Mutlu,[1,2,3,4] Pierre Lucas,[1,2] Krishna Muralidharan,[1,2] Andrea Alù,[2,5,6] Keith Runge,[1,2] and Pierre A. Deymier[1,2]

[1] *Department of Materials Science and Engineering, University of Arizona, Tucson, Arizona 85721, USA*
[2] *New Frontiers of Sound Science and Technology Center, University of Arizona, Tucson, Arizona 85721, USA*
[3] *Department of Electrical and Computer Engineering, University of Arizona, Tucson, Arizona 85721, USA*
[4] *Department of Physics, University of Arizona, Tucson, Arizona 85721, USA*
[5] *Photonics Initiative, Advanced Science Research Center, City University of New York, New York, New York 10031, USA*
[6] *Physics Program, Graduate Center, City University of New York, New York, New York 10016, USA*

(Received 14 November 2025; revised 24 February 2026; accepted 8 April 2026; published 13 May 2026)

This paper is a contribution to the Physical Review Applied collection titled Phononics and Metamaterials.

Consumer demand for next-generation telecommunication devices with increasing performance and miniaturization imposes strong constraints on radio-frequency (RF) surface-acoustic-wave (SAW) devices, such as low cost, low insertion loss, and a small footprint. We use COMSOL MULTIPHYSICS to investigate the properties of realistic RF SAW devices with a thin film located along the delay line between the source and detector interdigitated transducers on a 128° Y-cut lithium niobate (LN) substrate. In these simulations, a chalcogenide phase-change material, germanium antimony telluride, is chosen for the thin film material that could be converted to desired superlattices (SLs) constituted of crystalline and amorphous segments. Two types of SL configuration, with crystalline to amorphous segment ratios of 1:1 and 1:2, are investigated, and corresponding frequency responses are discussed. The primary outcome of this work is the demonstration of a SL RF duplexer and a topological acoustic narrow-band resonator in a SAW device that otherwise acts as a broadband filter. This work shows that a SL with thickness amounting to one tenth of the wavelength of the SAW can drastically affect the transmission of the composite device through mode hybridization between Bloch waves in the SL and the SAW in the LN substrate.

DOI: 10.1103/p8q7-r6ck

I. INTRODUCTION

Surface-acoustic-wave (SAW) devices have been commonly used in telecommunication systems as filters [1–4], resonators [5–10], sensors [11–15], and delay lines [16], and have proved their technological dominance over other technologies [17] in many scientific applications [14]. These miniaturized devices exploit the acoustic waves at much smaller wavelengths than electromagnetic waves in the telecommunication frequency bands. The working principle of SAW devices is based on the propagation of elastic waves along the surface of a piezoelectric substrate [e.g., lithium niobate (LN)] produced by an interdigitated transducer (IDT) fabricated on the surface of the substrate [16,18–20]. Among several design configurations of SAW devices, structures such as gratings and/or trenches inserted between input and output IDTs are used to manipulate the propagation of the SAW to improve performance and/or functionality [14,21–24]. SAW devices, however, despite their widespread applications in signal processing, sensing [11–13], and wireless communications [25], exhibit insertion loss [26], and have inherent limitations associated with their single functionality and lack of reconfigurability. SAW devices, which are massively used in consumer products, also require high-throughput fabrication [27]. Overcoming these limitations is crucial for the advancement of SAW-based technologies for next-generation communication such as low-cost, lossless, multifunctional, and reconfigurable radio-frequency (RF) systems [28].

Phononic crystals (PnC) exhibiting bandgaps [29,30] are the acoustic counterparts of photonic crystals [31,32]. After their fundamental studies, the research community

*Contact author: farrukhnajmi@arizona.edu

witnessed the exploitation of periodic structures that can give rise to forbidden acoustic bands and localized/hybridized acoustic resonances [33,34] due to variations in the mechanical and geometric properties of the acoustic metamaterials [34,35]. Benchabane *et al*. [36–39] have investigated and explained how pillared PCs can be used as stop-band and passband filters for SAWs depending on the periodicity of the structure. Ash *et al*. [40] have demonstrated a concept of finite-depth annular holes to act as a SAW PC to achieve a low-frequency bandgap in contrast to pillared configurations. A comprehensive introduction to and integration of PCs in SAW devices can be found in recently published review articles [41,42].

Recently, topological acoustic waves have received much attention for their extraordinary properties [42–45]. Of particular relevance is the occurrence of one-way propagating waves due to structural or temporal symmetry breaking. Modes at the edge of media with unconventional topology or modes at the interface of topologically different media may arise in two-dimensional (2D) phononic structures with broken inversion or parity symmetry [42, 46]. Breaking time-reversal symmetry can lead to bulk one-way propagating waves [47]. However, this typically requires active devices to enable time modulation or mechanical motion [48]. For instance, to break time reversal symmetry, rotational fluid mechanisms to mimic the magnetic field for phonons have been reported to develop the acoustic counterpart of Zeeman splitting [49], which may be exploited to enable topological effects in acoustics [35,50]. A passive approach for realizing one-way propagating bulk acoustic waves has been shown to result from resonance-induced translational symmetry-breaking in one-dimensional (1D) superlattices (SLs) [42].

SLs support Bloch waves due to their translational periodicity. The band structure of acoustic SLs exhibits alternating passing bands and bandgaps. Moreover, some of these passing bands support waves with nonconventional topology, i.e., with a Berry phase taking the value of π [51–53]. Passing bands with nonconventional topology arise from the coexistence of modes of vibrations with zero amplitude for some wave number and nonzero amplitude for the opposite wave number [53]. These modes, called "DRAK modes" [46], result from Fabry-Perot (FP) resonances that break the translational symmetry of Bloch waves in these periodic media [53]. Because of their one-way propagation features, DRAK modes may have the potential of increasing transmissivity of acoustic wave devices [52] such as RF SAW devices.

Producing structures with complex periodicity in elastic properties can be challenging. In that respect, phase-change materials (PCMs) such as germanium antimony telluride (GST) are known to exhibit strong contrast in physical properties between their crystalline and amorphous phases. Combined with their fast-switching capability, PCMs have been integral to nonvolatile data storage technologies such as rewritable digital video discs (DVDs) or personal computer random access memory (RAM). The large contrast in physical properties between the amorphous and crystalline phases of PCMs has been broadly exploited to encode binary information in semipermanent (nonvolatile) form. In data storage DVDs, the contrast in the reflectivity between the two phases of the PCM is exploited, while in personal computer RAM, the contrast in resistivity is exploited [54–57]. In addition to optical and electrical contrasts, GST materials exhibit significant differences in mechanical properties, including *density, Poisson's ratio, and Young's modulus*, between the crystalline and amorphous phases (see Table I). To the best of our knowledge, the contrast in mechanical attributes of PCMs and their reconfigurability have never been exploited to produce acoustic devices, but they should be an ideal candidate to realize multifunctional SL RF SAW devices.

TABLE I. Mechanical properties of the GST material in amorphous and crystalline phases.

Property	Amorphous	Crystalline
Density (kg/m^3) [58]	5860	6270
Young's modulus (GPa) [58]	18.9	38.2
Poisson's ratio [59]	0.3	0.26

In this work, we explore the integration of a SL on the surface of a standard RF SAW device as an approach to enhance its performance and functionality. Moreover, we use a SL composed of a PCM that would be compatible with high-throughput fabrication of SL RF SAW devices and also would endow the devices with the possibility of becoming reconfigurable. The proposed composite PCM-based SL RF SAW device geometry is illustrated in Fig. 1.

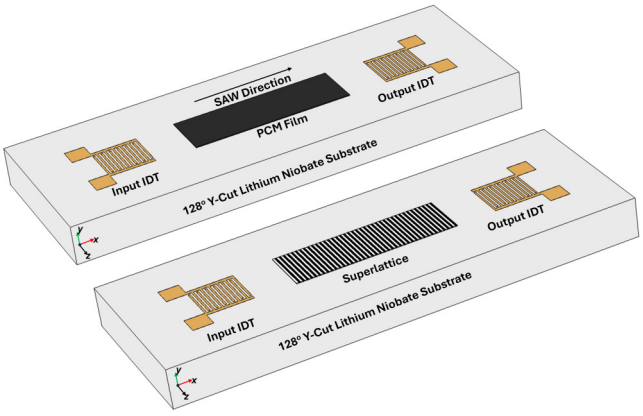

FIG. 1. Top: Composite SAW device with a thin PCM film of amorphous GST material located on a LN delay line. The dimensions of the GST amorphous film are 400, 2, and 115 μm along the x, y, and z directions, respectively. Bottom: Same but with a GST SL thin film composed of alternating crystalline and amorphous phases.

The proposed geometry consists of a thin layer of GST material (2 μm thick) located on the LN substrate in the delay line of the SAW device, with overall in-plane dimensions of 115 μm in width and 400 μm along the delay line. The GST layer is patterned as a SL composed of alternating crystalline and amorphous strips, with micron-scale strip widths (5 μm or greater). Because GST crystallization kinetics are nucleation-dominated, its metastable cubic crystalline phase is typically polycrystalline with grain sizes on the order of tens of nanometers [60,61]. Since this length scale is at least an order of magnitude smaller than the minimum feature size of the crystalline regions in the present design, we treat crystalline GST as effectively isotropic and use the corresponding elastic properties (e.g., Young's modulus and Poisson's ratio) and mass density listed in Table I.

The GST SL RF SAW device in Fig. 1 is simulated with the finite-element analysis (FEA) package COMSOL MULTIPHYSICS. FEA has proved to produce realistic simulations of such devices for optimized design [62–64]. To reduce computational overhead in FEA, we exploit the mirror symmetry across the x-y plane to reduce the simulation to a 2D analysis. A 2D model of the SAW device is shown in Fig. 2.

The aperture length of the Electrodes (i.e., IDT fingers) is not included in the 2D analysis. The 2D simulation gives physically realistic results as far as the resonance frequency, transmittance (i.e., potential at the output IDT), and displacement fields in the SL and LN substrate are concerned for the propagation of SAWs in the x direction. The period of the SL unit cell (UC) is defined as $d = d_c + d_a$, where d_c is the width of the crystalline region and d_a is the width of the amorphous region. Two representative SL configurations are analyzed: (1) a SL with $d_c = 5$ μm and $d_a = 5$ μm (UC size, $d = 10$ μm) and (2) a SL with $d_c = 5$ μm and $d_a = 10$ μm (UC size, $d = 15$ μm). These SLs are subsequently referred to as 5/5 and 5/10 SLs.

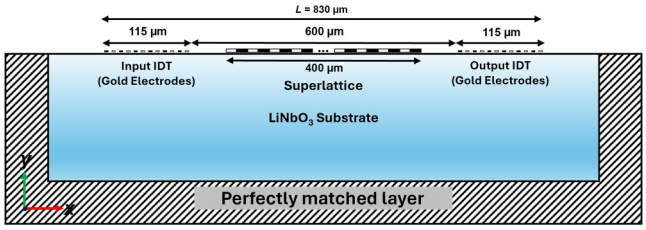

FIG. 2. 2D cross section of the three-dimensional device shown in Fig. 1 exploiting the mirror symmetry to perform FEA. PMLs have been applied to absorb the transmitted acoustic waves to prevent back-reflection from the boundaries of the device. Each IDT has 12 fingers of gold designed for the desired frequency.

II. METHOD

A 2D frequency-domain analysis, in the range from 150 to 250 MHz, is performed to investigate the propagation of acoustic waves in SAW devices. The SAW device is designed for a 200 MHz resonance frequency in which two gold IDTs, having 12 fingers each, have been deposited on the top of the LN substrate. The IDT fingers are 0.2 μm (200 nm) thick and 5 μm wide, with 5 μm spacing between them (periodicity 20 μm). The distance between the input IDT and the output IDT is 600 μm. In the case of composite SL SAW devices, a 2-μm-thick and 400-μm-long thin film of PCM is centered on the delay line. Perfectly matched layers (PMLs) are applied at the domain boundaries for wave absorption to prevent reflections from the device boundaries. Appropriate boundary conditions were set to simulate SAW excitation and propagation. The geometry was meshed with both triangular (substrate and film/SLs) and structural/rectangular (PMLs) meshing elements to balance computational efficiency and solution accuracy [65]. LN substrate with 128° Y-cut is used for simulations due to its high electromechanical coupling coefficient that generates an efficient SAW signal for strong propagation. A rotated coordinate system with Euler angles (0°, 38°, 0°) [66] is assigned to the substrate to align the crystal orientation with the global coordinate system of the device. An electrical potential (V_{in}) of 1 V is applied at the input IDT, and a potential probe is introduced at the output IDT to monitor the floating potential (V_{out}) produced by the propagated SAW. The frequency increment (the step size) is kept at 0.5 MHz, and results in convergence with reasonable accuracy. A comparison of the frequency response with a smaller step size (i.e., 0.1 MHz) is shown in Fig. 23 in Appendix F, validating the convergence of the solution.

III. RESULTS

FEA of the device with a free surface was performed, and the frequency response of the device was calculated, as shown in Fig. 3. A strong broadband signal ($\Delta f = 32$ MHz) of the SAW propagates through the delay line. Subsequently, FEAs of devices with three different configurations—namely, homogeneous GST thin film (crystalline or amorphous), 5/5 SL, and 5/10 SL–were performed. The corresponding results are discussed below.

A. SAW device with a homogeneous amorphous GST thin film in the delay line

A SAW device with a homogeneous amorphous GST thin film introduced between the input and output IDTs was simulated and compared with a SAW device with a free surface, as shown in Fig. 4. The SAW device with an amorphous film is meant to serve as a reference to characterize the performance of the device with SLs. It was

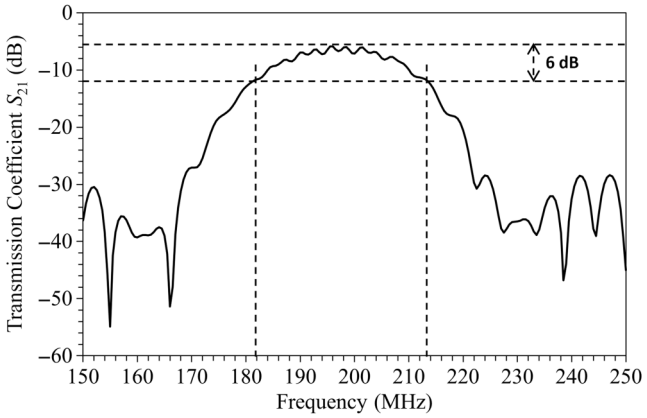

FIG. 3. Frequency response (transmission coefficient S_{21}) for the SAW device with a free surface. The absolute output potential is measured at the output IDT.

previously verified by FEA simulation that a thin film of 2 μm thickness provides a satisfactory balance between transmissivity and coupling with the LN SAW (see Fig. 16 in Appendix A). Indeed, a submicron film does not interact significantly with the SAW, while thicker films scatter the SAW and reduce significantly the output potential measured at the output IDT. In the case of the device with a 2-μm-thick layer, a small fraction of the SAW energy is scattered at the edge of the film on the input side. The output potential/transmission level is reduced by approximately −12 dB. The frequency response (transmission coefficient S_{21}) for the SAW device with a free surface is shown in Fig. 3.

Figure 4 shows that the devices with thin films exhibit ripples in the transmission spectrum, which can be assigned to partial reflection of SAWs from the film edges. The displacement field inside the device at the resonance frequency of 198.5 MHz, shown in Fig. 5 (top), indicates

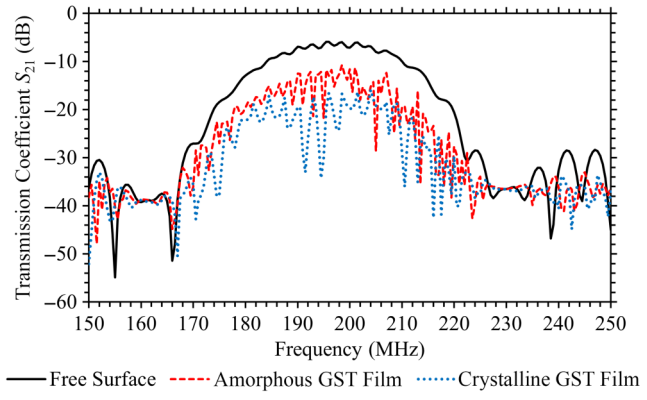

FIG. 4. Comparison of the frequency response of the SAW device between the FEA simulation results among the free surface (continuous black line), amorphous GST thin film (dashed red line), and crystalline GST thin film (dotted blue line).

that the SAW hybridizes with a propagative mode of the film (see Fig. 5, bottom). The propagating hybridized wave takes on a mixed character between a pure SAW and a pure guided thin film mode. The device acts as a passband filter in the range from about 180 MHz to about 210 MHz, with fluctuations in the passband that may be due to the localized trapping of the acoustic energy in the thin film. The amorphous GST film was then replaced with crystalline GST thin film and analyzed. The propagation of the SAW through the crystalline GST thin film is weaker than the propagation through the amorphous thin film due to leakage of film-propagative waves in LN resulting from the impedance match between crystalline GST film and the LN substrate. In the case of amorphous GST, the stronger mismatch stops the energy in the film from leaking in LN during the hybridized wave propagation.

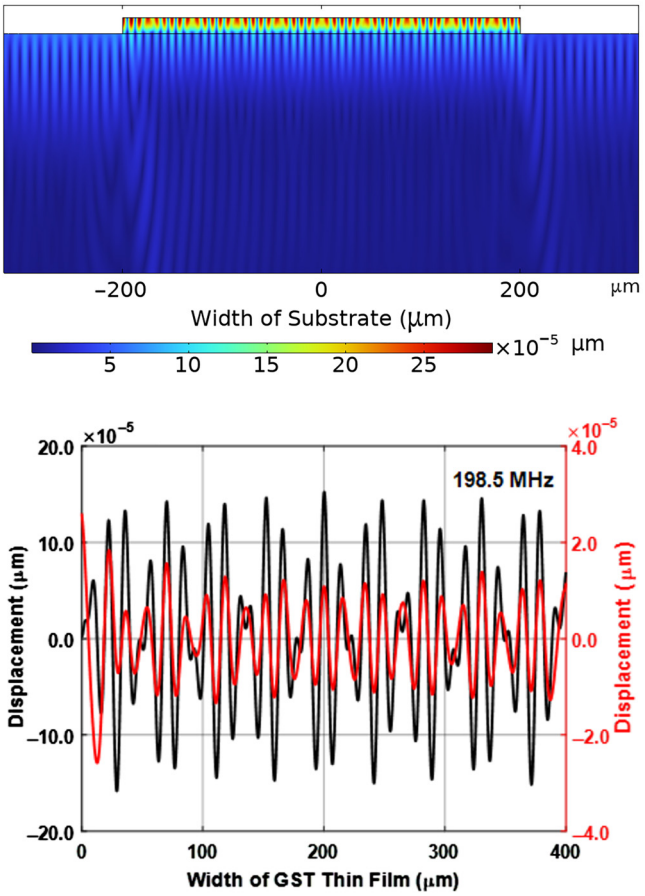

FIG. 5. Top: Total displacement field in the amorphous GST thin film at the resonance frequency (i.e., 198.5 MHz). Bottom: Magnitude of the x component of displacement at the top of the film (black line) and 1 μm inside the LN substrate (red line) as a function of the position along the thin film. The y components of the displacement in the thin film and the LN substrate are always in phase, indicating that they form a hybridized wave that propagates through the composite system.

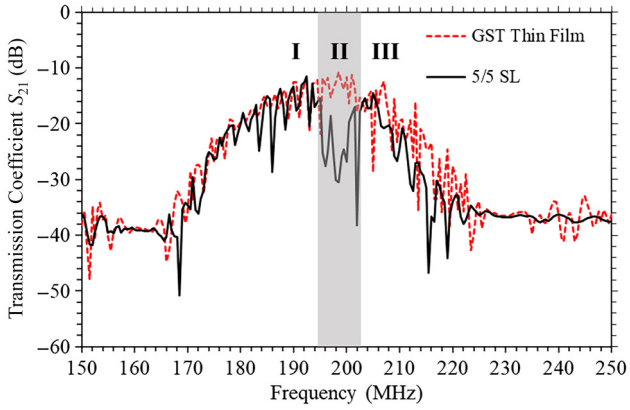

FIG. 6. Frequency response of the SAW device with a thin homogeneous film of amorphous GST (dotted red line) and with the 5/5 SL (continuous black line). The shaded region shows the bandgap. Three regions (I–III) have been segregated to discuss the evolution of the waves in the 5/5 SL.

B. SAW device with a 5/5 SL

We now consider a SL with crystalline and amorphous regions of 5 μm width each with 40 UCs. Figure 6 shows a comparison of the frequency response curves of the SAW device with the reference homogeneous amorphous GST film and of the SAW device with the 5/5 SL. We observe a strong drop in transmissivity at about 198.5 MHz. The 5/5 SL configuration has created a bandgap in the region where there previously was strong transmission in the GST thin film. This region is shown in grey in Fig. 6 and is referred to as "region II" for further discussion.

Figure 7 shows the displacement field in the SL/LN, and the displacement magnitude along the top of the 5/5 SL and inside the LN substrate for selected frequencies in the three regions shown in Fig. 6. Outside the transmission gap, the displacements inside the SL and the LN substrate are essentially in phase along the entire film, suggesting that the device supports propagating waves that are hybrids of SAWs in the LN and Bloch waves in the SL at frequencies of 192.5 MHz in region I and 205 MHz in region III. At frequencies inside the stop band, the localization of waves on the input side of the SL with exponentially decaying amplitude is characteristic of evanescent waves (198.5 MHz in region II). The evanescent waves in the SL are essentially in phase with the SAW in the LN beyond the first third of the film. These observations suggest that the observed transmission gap arises from hybridization between the SAW band and a folded SL band.

To illustrate the notion qualitatively, we used a simple mass-spring model composed of a (1D) Su-Schrieffer-Heeger (SSH) chain, representing the SL coupled elastically to a 1D single-mass harmonic chain representing the SAW-supporting LN substrate [Fig. 8(a)]. The choice of a discrete chain model is deliberate and made to obtain analytical solutions that can provide physical insight into the behavior of the SL/LN composite systems studied here.

In the model, we take intermass spacing equal to 1, and all masses are the same. The dynamical matrix for this system is shown in Eq. (B1) in Appendix B, and the band structure is shown in Fig. 8(b). In Appendix C, the analytical solutions of the discrete model of the SSH/monoatomic chain show that a SL possessing nonconventional topological characteristics (SSH

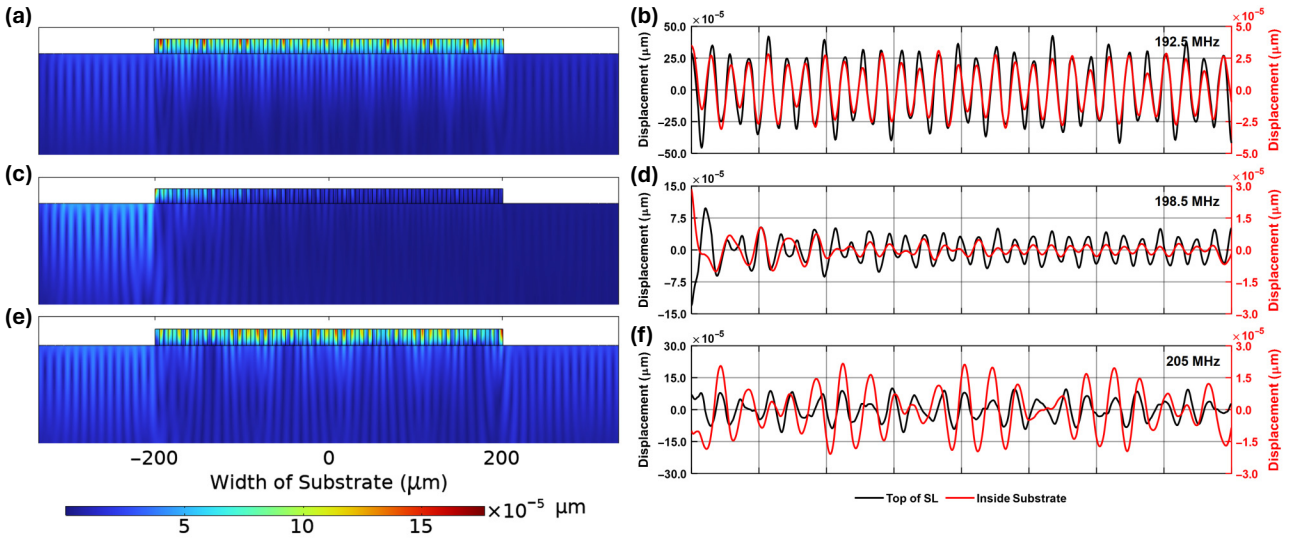

FIG. 7. Total displacement field in the SL/LN substrate, and displacement magnitude along the top of the 5/5 SL (black line) and 1 μm below the interface in the LN substate (red line) at the three frequencies chosen in each region: (a),(b) 192.5 MHz in region I, (c),(d) 198.5 MHz in region II, and (e),(f) 205 MHz in region III.

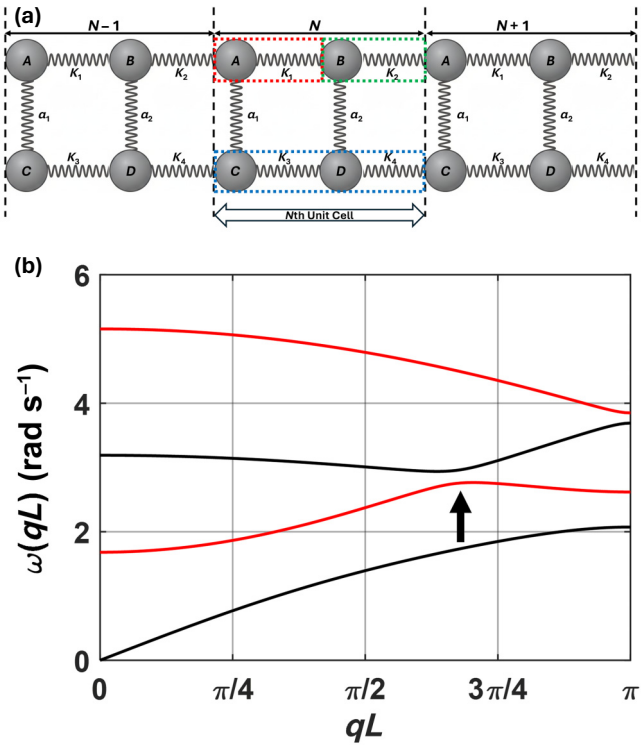

FIG. 8. (a). Schematic illustration of a SSH chain representing the 5/5 SL elastically coupled to a 1D single-mass harmonic chain representing the SAW-supporting LN substrate. K_1, K_2, and K_3 represent the square of the velocities of elastic waves in the crystalline, amorphous and LN substrate, respectively. α_1 and α_2 represent the square of the group velocities of elastic waves in the case of coupled crystalline/LN and amorphous/LN interfaces. (b) Calculated band structure. The black arrow indicates hybridization between a SAW LN band and the folded SL band. The band structures have been drawn with the use of relative velocities such that all velocities are a ratio with respect to $\alpha_2 = 1.6^2$. $K_1 = (2.7/1.6)^2$, $K_2 = (2.0/1.6)^2$, $K_3 = (4.0/1.6)^2$, $\alpha_1 = (2.2/1.6)^2$, $\alpha_2 = 1$, and $L = 2a$, where a is the distance between two masses.

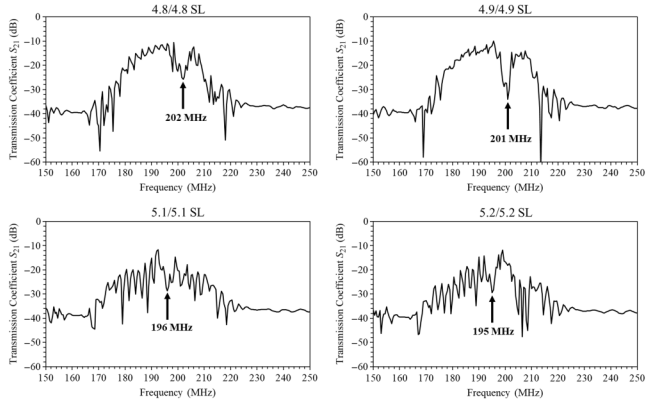

FIG. 9. Effect of the period of the GST SL for a UC with constant filling fraction of crystalline and amorphous regions. Transmission spectra for four SLs, 4.8/4.8 SL, 4.9/4.9 SL, 5.1/5.1 SL, and 5.2/5.2 SL, with a constant ratio of the UC size $d_c/d_a = 1:1$. An increase in the SL period decreases the bandgap frequency (arrow) in accordance with the band folding.

system) can endow a topologically conventional substrate (monatomic chain) with nonconventional topological character when elastically coupled.

To further confirm the origin of the transmission gap as a hybridization gap in the output potential, we simulated devices with variable periods but constant ratios of the crystalline and amorphous segment widths (i.e., $d_c = d_a$). Increasing the period decreases the edge of the Brillouin zone of the SL toward lower values, as shown in Fig. 9, subsequently decreasing the frequency at which the SAW band intersects a folded SL band, which is where the hybridization gap may occur.

C. SAW device with a 5/10 SL

Next we investigate a SL with 5-μm-wide crystalline segments and 10-μm-wide amorphous segments. The period is $d = 15$ μm, and the film is composed of 26 UCs. The frequency response curve of the composite SL SAW device is reported in Fig. 10, where it is compared with the frequency response curve of the reference device with a homogeneous GST amorphous thin film.

The frequency response of the device with the 5/10 SL exhibits three characteristic regions. First, passing bands below 200 MHz and above 208 MHz are associated with propagative hybrid SAW Bloch waves. Second, a very low signal between 202 and 208 MHz is associated with a stop band and evanescent waves. Third and most importantly, there is a very narrow transmission peak centered on the frequency of 200 MHz. The Q factor of this narrow transmission peak is approximately 222. The transmission level approaches that of the device with a homogeneous amorphous film in the delay line. A similar asymmetric transmission was observed in theoretical studies of DRAK

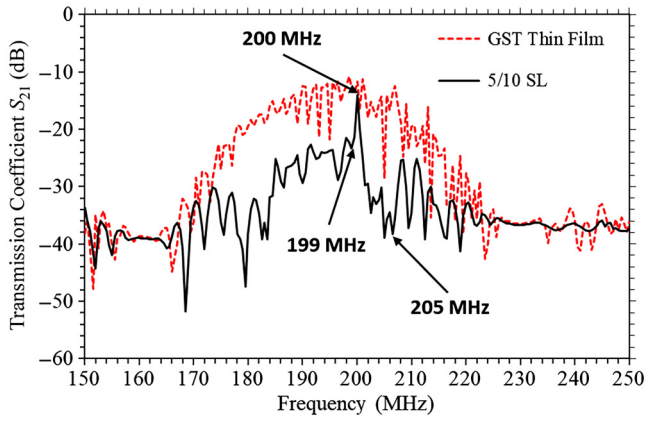

FIG. 10. Frequency response of the device with an amorphous GST film (dotted red line) and a 5/10 SL (continuous black line).

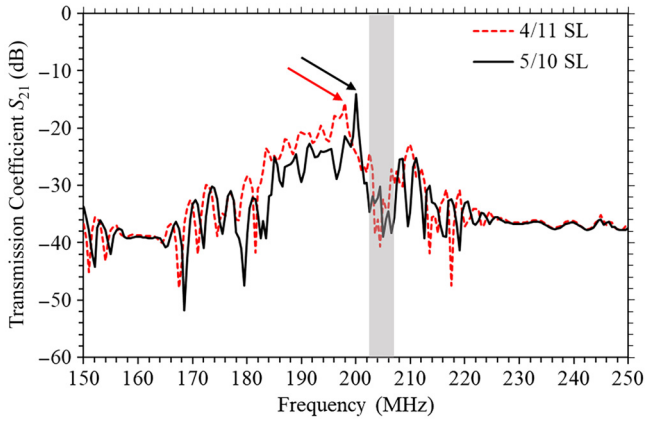

FIG. 11. Effect of the variation of the width of the crystalline/amorphous regions of the SL at constant period (UC size $d = 15$ μm) on the frequency response of the SL SAW device. The solid line corresponds to the 5/10 SL. The dotted line is for a 4/11 SL with $d_c = 4$ μm and $d_a = 11$ μm. The location of the bandgap (shaded region) shows no variation, while the DRAK peak moves to a lower frequency (red arrow).

modes in finite superlattices [52]. Both systems reported in Fig. 10 possess film edges that may lead to partial reflection. However, the very large contrast in the transmission of the 5/10 SL system compared with the homogeneous amorphous GST film shows unambiguously another effect in addition to partial reflection, which we attribute to the DRAK mode. Topologically unconventional passing bands in a finite SL show asymmetric shapes as a function of frequency. A passing band with nonconventional topology supports regions corresponding to Bloch wave propagation, and regions with very strong transmission associated with a DRAK mode. The FP resonance that breaks the translational symmetry of Bloch waves in periodic media, a condition for the existence of a DRAK mode within a passing band, is $\sin k_a d_a = 0$. The wave number in the amorphous region, k_a, is defined by the relation $k_a = \omega/c_a$, with c_a being the speed of the wave in the amorphous region. This condition can be reformulated as $k_a d_a = m\pi$, where m is an integer. The frequencies at which DRAK modes may occur are therefore given by $\omega = m\pi c_a/d_a$. This latter condition indicates that the frequency of the resonance yielding a DRAK mode decreases inversely proportionally to the length of the amorphous segment in the SL at fixed period d. This condition is confirmed in Fig. 11 from comparison of the frequency response of the SAW device with a 5/10 SL and a 4/11 SL (i.e., with $d_c = 4$ μm and $d_a = 11$ μm). The sharp transmission peak shifts to a lower frequency (red arrow in Fig. 11) as the length d_a of the amorphous region increases. Note that the frequency at which the bandgap occurs is not affected since the total period remains constant (i.e., $d = 15$ μm). Further evidence for a hybridization between a resonance in the SL and the SAW giving rise to the narrow transmission is shown in Fig. 12, which shows the displacement field

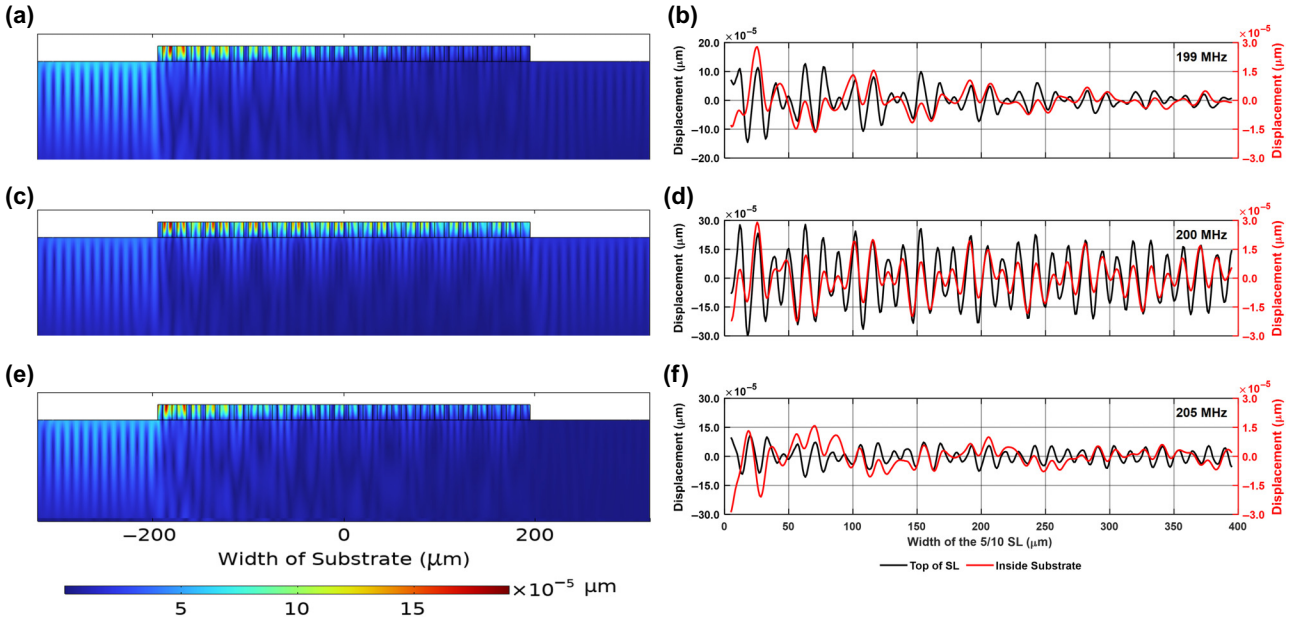

FIG. 12. Total displacement field in the LN/SL and 5/10 SL at the three frequencies chosen. (a) The displacement field in the device at 199 MHz and the displacement magnitude measured at the top of the 5/10 SL (black line) and 1 μm below the interface in the LN substate (red line). (c),(d) and (e),(f) Displacement field in the SL/LN and displacement magnitude at the top of the SL at 200 and 205 MHz, respectively. A large amplitude in the 5/L SL at 200 MHz is indicative of a resonance, whereas the weak transmission at 205 MHz shows a bandgap.

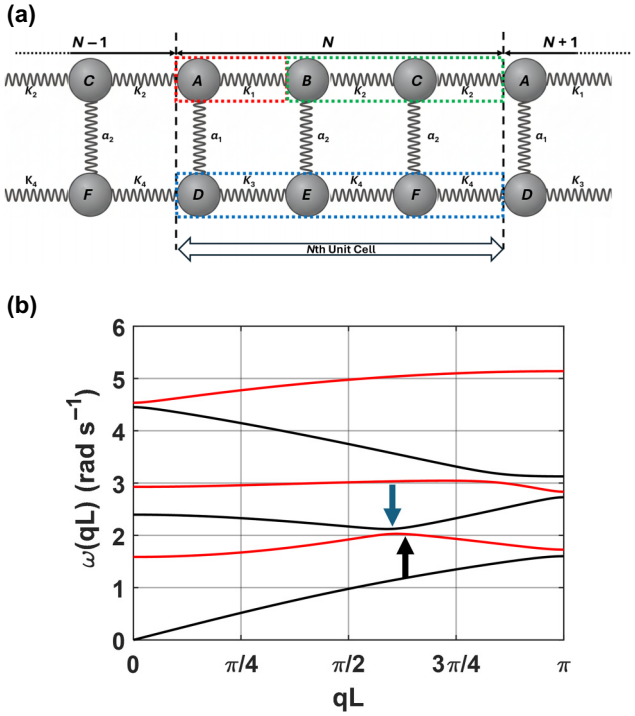

FIG. 13. (a) Schematic illustration of a SL chain representing the 5/10 SL elastically coupled to a 1D single-mass harmonic chain representing the SAW-supporting LN substrate. (b) Calculated band structure. The blue arrow indicates hybridization between a SAW LN band and the folded SL band. The black arrow marks the location of the DRAK mode on the first folded band (second band) of the SL chain. The band structures have been drawn with the use of relative velocities as given in the caption for Fig. 8(b). $L = 3a$, where a is the distance between two masses.

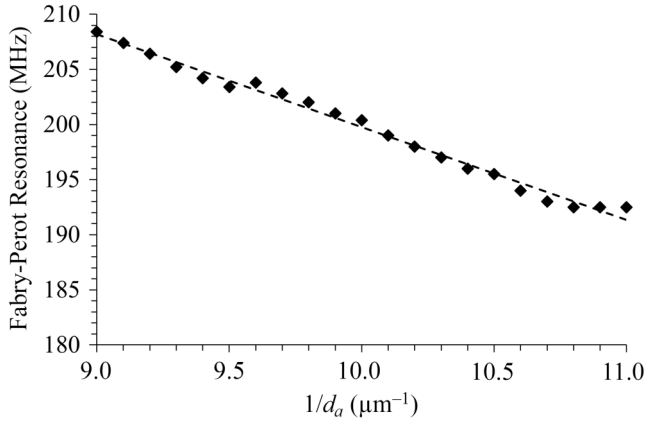

FIG. 14. Resonance frequency as a function of the reciprocal of the width of the amorphous segment with the crystalline segment kept constant (diamonds). The dashed line is the linear fitting of the data representing a linear relation between the FP resonance and the width of the amorphous segment in the SL, where the term $m\pi c_a/2\pi$ represents the slope of the curve.

in the SL/LN and the displacement magnitude at the top of the SL (black curves) and 1 μm inside the LN substrate (red curves) for three frequencies. At a frequency of 200 MHz, the magnitude of the displacement field inside the SL is large, and the waves in both the SL and the LN substrate are in phase, as shown in Fig. 12(d). The displacement field as a function of position along the SL shows a small, nearly linear decrease, which is attributed to leakage of energy into the LN substrate as the resonant wave propagates.

Further qualitative insight into these observations is obtained by considering another composite mass-spring model constituted of a 1D SL chain where the UC is now composed of three springs, two of which are identical (amorphous segment) and one of them is different (crystalline segment), elastically coupled to the 1D single-mass harmonic chain representing the SAW-supporting LN substrate, as shown in Fig. 13(a). The dynamical matrix for this system is shown in Eq. (B2) in Appendix B, and the band structure is shown in Fig. 13(b).

This model indicates qualitatively that the observed transmission gap may arise from hybridization between the SAW band and the first folded SL band. The close proximity of the DRAK mode to the hybridization gap also suggests that the FP resonance may hybridize significantly with the SAW. To further confirm the DRAK mode origin of the narrow transmission peak in the 5/10 SL device, we note that the FP resonance condition implies that $\omega = 2\pi f = m\pi c_a/d_a$, with f being a linear function of the inverse of the width d_a of the amorphous segment, as shown in Fig. 14. The detailed analysis of the occurrence of DRAK modes in the coupled system is discussed in Appendix D.

It is noteworthy, and well supported in the established literature, that periodic gratings made of metal strips or grooves reflect SAWs through Bragg scattering [67,68]. This is also the case for our 5/5 SL, which exhibits a bandgap resulting from periodicity. However, in the case of our 5/10 SL, the transmission is affected by a physical phenomenon (DRAK mode), which, as far as we know, has not been reported to date in periodic gratings.

D. Topology of composite systems

In Sec. III B we showed that a 5/5 SL possessing nonconventional topological characteristics (SSH system) can endow a topologically conventional substrate with nonconventional topological character when elastically coupled. In Appendix D, we address the topology of a 5/10 SL coupled with a homogeneous LN substate. For this, we consider the model in Fig. 13(a) and explore the existence of DRAK modes in the coupled system. Appendix D discusses the mathematical formulation and detailed analysis of the composite system. We show the existence of DRAK modes in the coupled system with zero amplitudes on the negative side of Block wave vectors and

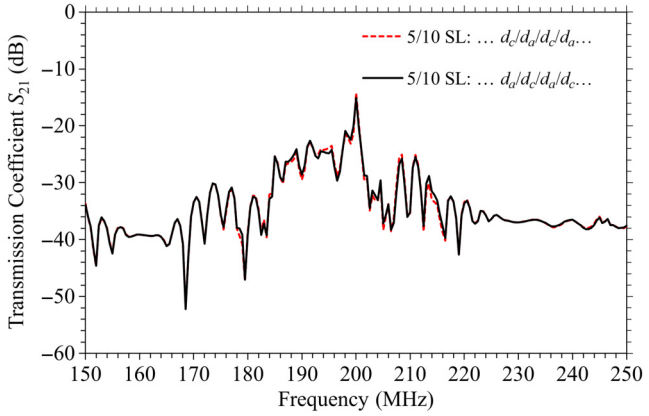

FIG. 15. Frequency response of a SAW device with a 5/10 SL... $d_c/d_a/d_c/d_a$... (solid black line) and a SL ... $d_a/d_c/d_a/d_c$... (dotted red line) with $d_a = 10$ μm and $d_c = 5$ μm. Overlapping of the response indicates reciprocity.

nonzero amplitudes on the positive side. These DRAK modes demonstrate the possibility of one-way propagation of the hybridized Block waves in the SL/LN composite system. It is known that DRAK modes are associated with bands with nonconventional topology in one-dimensional SLs [51–53,69]. A DRAK mode can add a contribution of π to the Berry phase of its supporting band. The model in Appendix D suggests the same possibility for a SL/LN composite system. It is therefore possible for a thin binary SL of GST material deposited on a LN substrate supporting a localized SAW to lead to topologically nontrivial waves through mode hybridization.

E. Reciprocity

Reciprocity in acoustic SLs ensures that the transmission characteristics remain invariant when the direction of wave propagation is reversed in the system. Previous theoretical studies of DRAK modes have shown that they obey reciprocity, since time reversal symmetry is not broken. To validate the reciprocity of the DRAK mode in the composite SL RF SAW device, we swap the input IDT and the output IDT. Numerically, the IDTs are kept the same, but the SL is redesigned such that on the input side it starts with an amorphous segment of 10 μm and then a crystalline segment of 5 μm. The SL is then constituted of 26 such UCs. Figure 15 validates the reciprocal behavior of the DRAK mode.

IV. DISCUSSION AND OUTLOOK

FEA simulations of composite SAW devices supporting structured thin films of GST in their delay line demonstrate the possibility of controlling the frequency response of the device with acceptable reduction in transmissivity. The SAW device with a 5/5 SL exhibits a hybridized bandgap separating two passing bands. This system offers a possible approach to designing SAW duplexers without increasing the device footprint, as current duplexers require two sets of input IDTs [70,71]. The SAW device with a 5/10 SL is an example of how FP resonance can enhance the performance of RF SAW filters/resonators. Indeed, FP resonances that break the translational symmetry of Bloch waves in periodic media may lead to one-way propagating DRAK modes, having the potential of increasing transmissivity of acoustic wave devices. By exploiting the nonconventional properties of resonant DRAK modes, one can narrow the passing band and increase the quality factor Q by nearly 2 orders of magnitude without increasing the device footprint or sacrificing the transmissivity significantly. Conventionally, to achieve narrow bandwidth without structuring the delay line of the device, one needs to increase the number of IDT fingers, subsequently increasing the device footprint and further hindering the scalability/miniaturization of SAW devices [72] (see Fig. 22 in Appendix E). The topological SAW filter designed in the present work is the first of its kind to narrow the passing band through a SL FP resonance, thus increasing significantly the device Q factor without increasing its footprint, while retaining high acoustic energy propagation. To quantify these benefits, we introduce the dimensionless figure of merit (FOM) $M = Q \times (V_{\text{out}}/V_{\text{in}}) \times \lambda/L$, where λ is the wavelength and L is the linear footprint measured from IDTs from end to end. The dimensionless FOM enables comparison of our devices with devices designed for different ranges of frequencies. For instance, structuring the delay line with tapered trenches has been shown to lead to a device with an extremely high Q factor [73]. However, the increase in Q is achieved at the cost of a very small acoustic energy propagation in the range from −40 to −50 dB [73]. The FOM of the composite SL RF SAW device with the 5/10 SL is 1.58. Using available data from Ref. [73], we estimate the FOM of the reported PC-based gigahertz device to be 0.61. The FOM of the SL RF SAW device is 2.6 times greater than that of the PC-based SAW resonator.

Furthermore, the choice of GST, a widely used PCM in optical storage and phase-change memory technologies, is motivated by its reversible switching between amorphous and crystalline phases and the strong contrast in mechanical properties between these phases (Table I). Importantly, prior work has demonstrated reliable formation of micron-scale crystalline/amorphous domains in GST thin film by both laser irradiation [74] and electrically driven, localized Joule heating [75,76]. Its switching capability suggests the possibility of manufacturing reconfigurable GST-based SL RF SAW devices. However, electrically driven reconfigurability would require electrodes that may impact the wave propagation, while laser irradiation would provide a noncontact method for reconfiguration. This work presents a realistic numerical demonstration of an acoustic device leveraging the unique characteristics of PCMs and unconventional acoustics waves in a SL coupled with SAWs,

opening a new frontier for their technological applications.

ACKNOWLEDGMENT

This work was supported by the Science and Technology Center New Frontiers of Sound through U.S. National Science Foundation Cooperative Agreement No. 2242925.

DATA AVAILABILITY

The data that support the findings of this article are not publicly available. The data are available from the authors upon reasonable request.

APPENDIX A: EFFECT OF THICKNESS OF THIN FILM

Figure 16 shows the effective thickness of the thin film that interacts significantly with the SAW propagating in LN.

Metal gratings are commonly used to control the propagation of waves in SAW devices. In this case the metal strip thickness can be a few hundredths of the wavelength owing to the large contrast in elastic properties of the substrate, metal, and air. Here the relatively small difference in elastic properties of the LN and amorphous and crystalline GST requires thicker films to impact the propagation of the SAW.

APPENDIX B: DYNAMICAL MATRICES OF THE MASS-SPRING SYSTEM REPRESENTING 5/5 SL AND 5/10 SL COMPOSITE SYSTEMS

The dynamical matrices for composite systems [Figs. 8(a) and 13(a)] composed of mass-spring models constituted of a 1D SL coupled elastically to a 1D single-mass harmonic chain representing the composite 5/5 SL and 5/10 SL SAW-supporting LN substrate are found analytically and are shown in Eqs. (B1) and (B2), respectively:

$$\overbrace{\begin{pmatrix} -m\omega^2+K_1+K_2+\alpha_1 & -K_1-K_2\exp(-iqL) & -\alpha_1 & 0 \\ -K_1-K_2\exp(iqL) & -m\omega^2+K_1+K_2+\alpha_2 & 0 & -\alpha_2 \\ -\alpha_1 & 0 & -m\omega^2+2K_3+\alpha_1 & -K_3-K_3\exp(-iqL) \\ 0 & -\alpha_2 & -K_3-K_3\exp(iqL) & -m\omega^2+2K_3+\alpha_2 \end{pmatrix}}^{M} \begin{pmatrix} A \\ B \\ C \\ D \end{pmatrix} = 0, \tag{B1}$$

$$\overbrace{\begin{pmatrix} -m\omega^2+K_1+K_2+\alpha_1 & -K_1 & -K_2\exp(-iqL) & -\alpha_1 & 0 & 0 \\ -K_1 & -m\omega^2+K_1+K_2+\alpha_2 & -K_2 & 0 & -\alpha_2 & 0 \\ -K_2\exp(iqL) & -K_2 & -m\omega^2+2K_2+\alpha_2 & 0 & 0 & -\alpha_2 \\ -\alpha_1 & 0 & 0 & -m\omega^2+2K_3+\alpha_1 & -K_3 & -K_3\exp(-iqL) \\ 0 & -\alpha_2 & 0 & -K_3 & -m\omega^2+2K_3+\alpha_2 & -K_3 \\ 0 & 0 & -\alpha_2 & -K_3\exp(iqL) & -K_3 & -m\omega^2+2K_3+\alpha_2 \end{pmatrix}}^{M} \begin{pmatrix} A \\ B \\ C \\ D \end{pmatrix} = 0. \tag{B2}$$

APPENDIX C: TOPOLOGY OF THE 5/5 SL COMPOSITE SYSTEM CONSTITUTED OF NONTRIVIAL AND TRIVIAL PARTS

For mathematical simplicity, we investigate the composite system shown in Fig. 8(a) and solve it analytically to determine the eigenvectors for the subsequent calculation of the Berry phase to investigate the topological features of the waves through the composite system. We make the following substitutions in Eq. (B1) for all the calculations [a unity mass ($m = 1$) is considered]:

$$\alpha_1 = \alpha_2 = \alpha,$$

$$\gamma_1 = -m\omega^2 + K_1 + K_2 + \alpha,$$

$$\gamma_2 = -m\omega^2 + 2K_3 + \alpha,$$

$$\delta = K_1 + K_2\exp(iqL),$$

$$\delta' = K_3 + K_3\exp(iqL).$$

This results in

$$\overbrace{\begin{pmatrix} \gamma_1 & -\delta^* & -\alpha & 0 \\ -\delta & \gamma_1 & 0 & -\alpha \\ -\alpha & 0 & \gamma_2 & -\delta'^* \\ 0 & -\alpha & -\delta' & \gamma_2 \end{pmatrix}}^{M} \begin{pmatrix} A \\ B \\ C \\ D \end{pmatrix} = 0. \tag{C1}$$

To obtain a tractable insightful analytical solution, we consider a special case,

$$K_1 = \beta + \varepsilon,$$

$$K_2 = \beta - \varepsilon,$$

$$K_3 = \beta + \varepsilon',$$

$$K_4 = \beta - \varepsilon',$$

such that $\gamma_1 = \gamma_2 = \gamma$.

With this, the dispersion relation (C2) is calculated by determinationdet$(M) = 0$ of Eq. (C1) and the dispersion plot is drawn in Fig. 17:

$$\gamma = [\pm]\sqrt{\frac{|\delta'|^2 + |\delta|^2 + 2\alpha^2(\pm)\sqrt{\left(|\delta'|^2 - |\delta|^2\right)^2 + 4\alpha^2|\delta + \delta'|^2}}{2}}. \tag{C2}$$

The normalized eigenvectors are found analytically as follows:

$$\mathbf{S} = \frac{1}{\sqrt{2(AA^* + CC^*)}} \begin{pmatrix} A \\ [\pm]A^* \\ C \\ [\pm]C^* \end{pmatrix}, \tag{C3}$$

with

$$\begin{aligned} A &= \frac{\alpha}{\gamma^2 - \delta\delta^*}\left([\pm]\gamma\sqrt{\delta'^* - \frac{Z}{\delta+\delta'}} + \delta^*\sqrt{\delta' - \frac{Z}{\delta^*+\delta'^*}}\right), \\ B &= [\pm]A^*, \\ C &= [\pm]\sqrt{\delta'^* - \frac{Z}{\delta+\delta'}}, \\ D &= [\pm]C^*, \end{aligned} \tag{C4}$$

where

$$Z = \frac{\delta'\delta'^* - \delta\delta^*(\mp)\sqrt{\left(|\delta|^2 - |\delta'|^2\right)^2 + 4\alpha^2|\delta + \delta'|^2}}{2}.$$

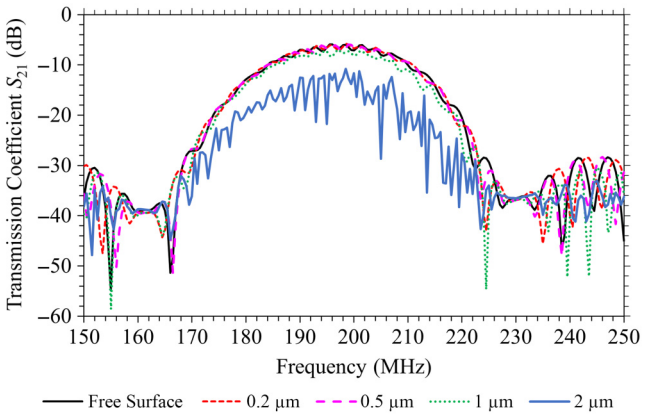

FIG. 16. Effect of the thickness of the amorphous GST thin film (the width of film along the delay line is 400 μm) on the SAW propagation in LN. There is no significant coupling between the film and the LN substrate for thicknesses less than or equal to 1 μm. Subsequently, a thickness of 2 μm of the amorphous GST thin film and both SLs is considered for all simulations reported in this paper in order to achieve significant coupling with the SAW.

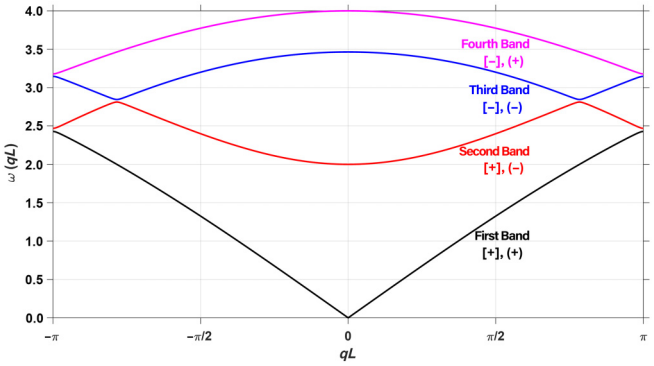

FIG. 17. Band structure of the coupled mass-spring system shown in the Fig. 8(a) plotted for $\varepsilon = \pm 0.1$, exhibiting hybridized bandgaps at $x_o = qL = \pm 2.46301$. The symbols in the brackets and parentheses are from the dispersion relation for γ, i.e., Eq. (C2).

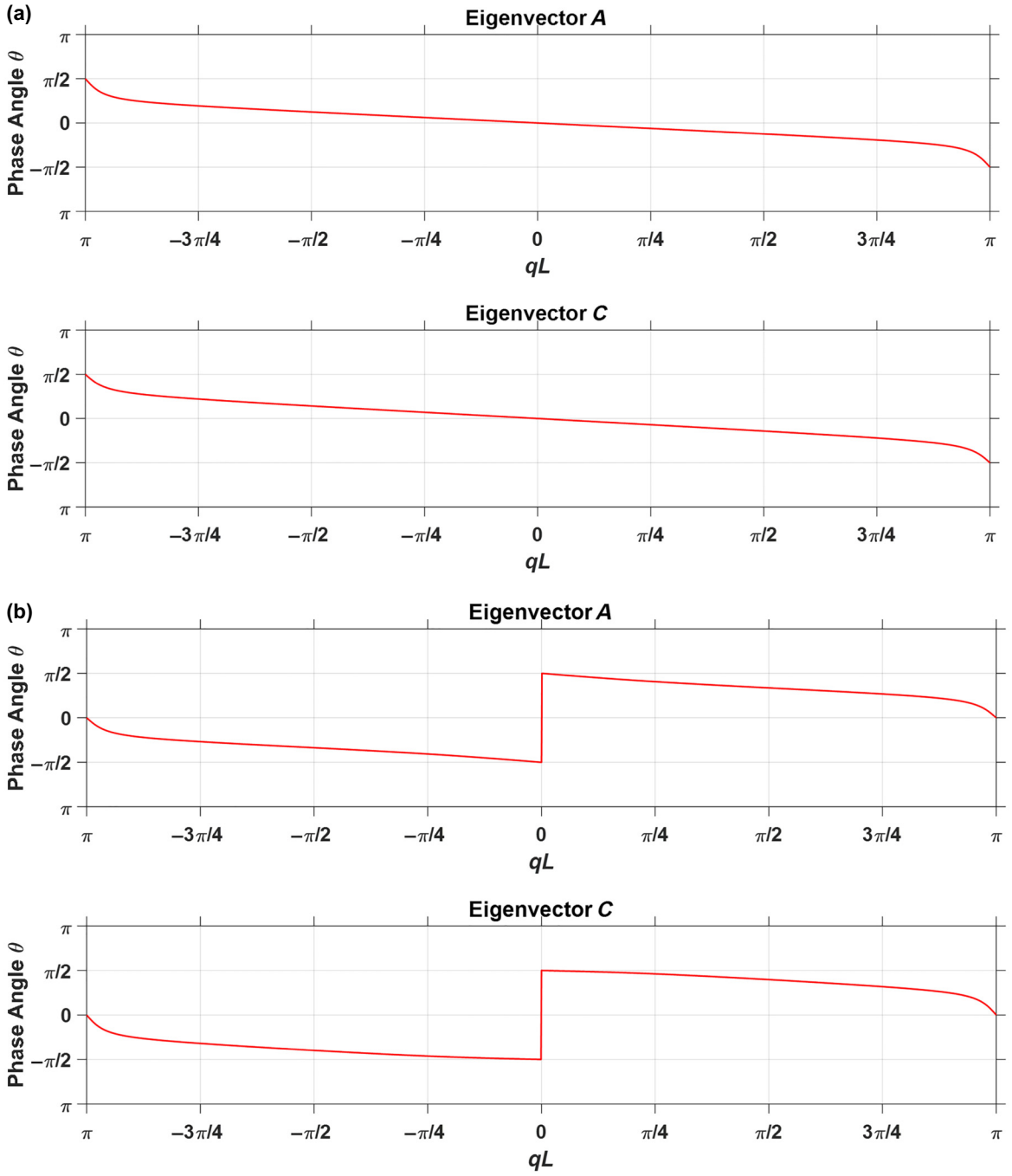

FIG. 18. Phase angles for eigenvectors A and C for $\varepsilon = 0.1,\ \varepsilon' = -0.2,$ and $\alpha = 2.5$: (a) first band; (b) second band.

The contribution of the continuous phase angle of the eigenvectors to the Berry connection (BC) is calculated to be

$$\mathbf{A}(qL) = iS^{T*}\frac{\partial S}{\partial(qL)} = 0. \tag{C5}$$

However, the eigenvectors exhibit discontinuities within the Brillouin zone. We need to account for the contribution of the discontinuities to the BC. For this let us consider a discontinuity at $x_o = qL$.

We can rewrite the **S**-vector as

$$\mathbf{S}(x_o) = \frac{1}{2}\begin{pmatrix} \exp(i\theta_a(x_o)) \\ [\pm]\exp(-i\theta_a(x_o)) \\ \exp(i\theta_c(x_o)) \\ [\pm]\exp(-i\theta_c(x_o)) \end{pmatrix}.$$

TABLE II. Determination of phase contributions to the Berry phase due to discontinuities in the first and second bands.

First band [+] (+)	Second band [+] (−)
At $x_o = qL = \pm\pi$	At $x = qL = \pm\pi$
$\cos\Delta\eta(x_o = \pm\pi) = \frac{1}{2}\left(\cos\left[\frac{\pi}{2} - \left(-\frac{\pi}{2}\right)\right] + \cos\left[\frac{\pi}{2} - \left(-\frac{\pi}{2}\right)\right]\right)$	$\Delta\eta(x_o = \pm\pi) = 0$
$\cos\Delta\eta(x_o) = \frac{1}{2}(\cos[\pi] + \cos[\pi])$	At $x_o = qL = 0$
$\Delta\eta(x_o) = \pi$	$\cos\Delta\eta(x_o = 0) = \frac{1}{2}\left(\left[\frac{\pi}{2} - \left(-\frac{\pi}{2}\right)\right] + \cos\left[\frac{\pi}{2} - \left(-\frac{\pi}{2}\right)\right]\right)$
	$\cos\Delta\eta(x_o) = \frac{1}{2}(\cos[\pi] + \cos[\pi])$
	$\Delta\eta(x_o) = \pi$

The **S**-vector near the discontinuity to within a small variation μ takes the form

$$\mathbf{S}(x_o \pm \mu) = \frac{1}{2}\begin{pmatrix} \exp(i\theta_a(x_o \pm \mu)) \\ [\pm]\exp(-i\theta_a(x_o \pm \mu)) \\ \exp(i\theta_c(x_o \pm \mu)) \\ [\pm]\exp(-i\theta_c(x_o \pm \mu)) \end{pmatrix}.$$

We can calculate the product,

$$\mathbf{S}^{T*}(x_o - \mu)S(x_o + \mu) = \frac{1}{2}(\cos[\theta_a(x_o + \mu) - \theta_a(x_o - \mu)] + \cos[\theta_c(x_o + \mu) - \theta_c(x_o - \mu)]).$$

If we define the change in geometric phase $\Delta\eta(x_o)$ as

$$\mathbf{S}^{T*}(x_o - \mu)S(x_o + \mu) = \exp i\Delta\eta(x_o) = \cos\Delta\eta(x_o) + i\sin\Delta\eta(x_o),$$

we will have a solution if $\Delta\eta = 0, \pm\pi, \pm 2\pi, \ldots$, i.e.,

TABLE III. Berry Phase calculations for different combinations of model parameters.

Values	Condition	Band no.	Berry phase (analytical solution)
$\beta = 1$	$\varepsilon' + \varepsilon < 0$	4 [−] (+)	π
$\varepsilon = 0.1$		3 [−] (−)	0
$\varepsilon' = -0.2$		2 [+] (−)	0
$\alpha = 0.5$		1 [+] (+)	π
$\beta = 1$	$\alpha > 2\,\beta$	4 [−] (+)	π
$\varepsilon = 0.1$		3 [−] (−)	π
$\varepsilon' = -0.2$		2 [+] (−)	π
$\alpha = 2.5$		1 [+] (+)	π
$\beta = 1$	$\varepsilon' + \varepsilon < \frac{\sqrt{(\varepsilon'^2 - \varepsilon^2)^2 + \alpha^2(\varepsilon + \varepsilon')^2}}{\varepsilon + \varepsilon'}$	4 [−] (+)	0
$\varepsilon = 0.1$		3 [−] (−)	π
$\varepsilon' = 0.2$		2 [+] (−)	π
$\alpha = 0.5$		1 [+] (+)	0

$$\cos\Delta\eta(x_o) = \frac{1}{2}(\cos[\theta_a(x_o + \mu) - \theta_a(x_o - \mu)] + \cos[\theta_c(x_o + \mu) - \theta_c(x_o - \mu)]). \quad \text{(C6)}$$

For instance, the Berry phase has been calculated for the eigenvector corresponding to the first and second bands in the case of $\varepsilon = 0.1$, $\varepsilon' = -0.2$, and $\alpha = 2.5$. Figures 18(a) and 18(b) shows the phases for $\theta_a(x = qL)$ and $\theta_c(x = qL)$ for first and second bands, respectively. These phases exhibit several discontinuities within $x = qL = \pm\pi$. The contributions to the Berry phase by these discontinuities are given in Table II.

The Berry phase contribution due to discontinuities in all bands for different values of ε, ε', and α is given in Table III, where the parametric study reveals the topologically trivial and nontrivial bands.

APPENDIX D: TOPOLOGY OF THE 5/10 SL COMPOSITE SYSTEM CONSTITUTED OF NONTRIVIAL AND TRIVIAL PARTS

To explain the existence of topological features in the 5/10 SL composite system, we develop a coupled mass-spring system, where the UC of the upper chain comprises the sequence of stiffnesses K_1, K_2, K_2, denoted the "K1-K2-K2 subsystem" and the corresponding UC in the lower chain with stiffnesses K_3, K_4, K_4, called the "K3-K4-K4

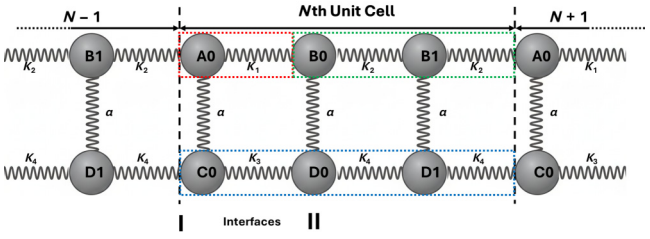

FIG. 19. Mass-spring system of the K1-K2-K2 chain coupled with the K3-K4-K4 chain through α. This system is representative of a composite system of 5/10 SL deposited on LN substrate.

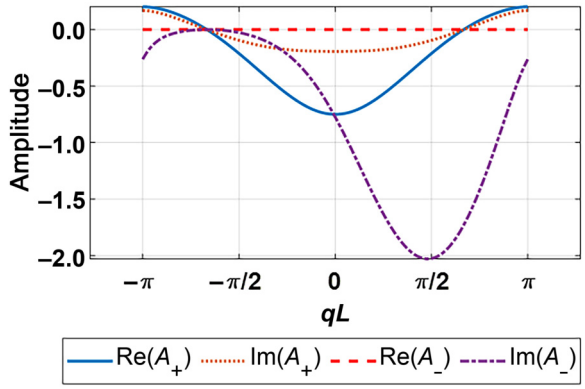

FIG. 20. Amplitudes of the real and imaginary parts of A_+ and A_- plotted for $K_1 = 2$ and $K_2 = 1$. The plot clearly shows zero amplitudes on the negative side of qL and nonzero amplitudes on the positive side, which is associated with the FP resonance due to the condition $\sin k_2 d_2 = 0$ and reflects the nonconventional topology of band 2.

subsystem," as shown in Fig. 19. The period of the system is given as $L = d_1 + d_2 = 3a$, where $d_1 = a$ and $d_2 = 2a$, with a the intermass spacing. The masses in the two subsystems are coupled via springs of stiffness α. This coupled mass-spring model is used as a representation of the composite system of 5/10 SL deposited on the LN substrate if $K_3 = K_4$ and is shown in Fig. 19.

The bulk equations of motion of the system described above can be written as follows:

$$\frac{d^2u^N_{A,m}}{dt^2} = K_1(u^N_{A,m+1} - u^N_{A,m}) - K_1(u^N_{A,m} - u^N_{A,m-1}),$$

$$\frac{d^2u^N_{B,l}}{dt^2} = K_2(u^N_{B,l+1} - u^N_{B,l}) - K_2(u^N_{B,l} - u^N_{B,l-1}),$$

$$\frac{d^2u^N_{C,m}}{dt^2} = K_3(u^N_{C,m+1} - u^N_{C,m}) - K_3(u^N_{C,m} - u^N_{C,m-1}),$$

$$\frac{d^2u^N_{D,l}}{dt^2} = K_4(u^N_{D,l+1} - u^N_{D,l}) - K_4(u^N_{D,l} - u^N_{D,l-1}). \quad \text{(D1)}$$

We seek solutions of the above equations in the form of superpositions of forward-propagating and backward-propagating plane waves in the four homogeneous chains with stiffnesses K_1, K_2, K_3, and K_4, where A_+, B_+, C_+, and D_+ represent the amplitude in the forward direction, and A_-, B_-, C_-, and D_- represent the amplitudes of the backward-propagating waves.

$$\begin{aligned} u^N_{A,m} &= e^{iqNL}(A_+e^{ik_1ma} + A_-e^{-ik_1ma})e^{i\omega t}, \\ u^N_{B,l} &= e^{iqNL}(B_+e^{ik_2la} + B_-e^{-ik_2la})e^{i\omega t}, \\ u^N_{C,m} &= e^{iqNL}(C_+e^{ik_1ma} + C_-e^{-ik_1ma})e^{i\omega t}, \\ u^N_{D,l} &= e^{iqNL}(D_+e^{ik_2la} + D_-e^{-ik_2la})e^{i\omega t}, \end{aligned} \quad \text{(D2)}$$

where k_1, k_2, k_3, and k_4 are the wave vectors of the acoustic waves propagating through the infinite harmonic chains; their values can be found from the dispersion relations

$$\omega^2 = 4K_j\left(\sin k_j \frac{a}{2}\right)^2 \Rightarrow k_j = \frac{2}{a}\sin^{-1}\left(\frac{\omega}{2\sqrt{K_j}}\right), \quad \text{(D3)}$$

where $j = 1 - 4$.

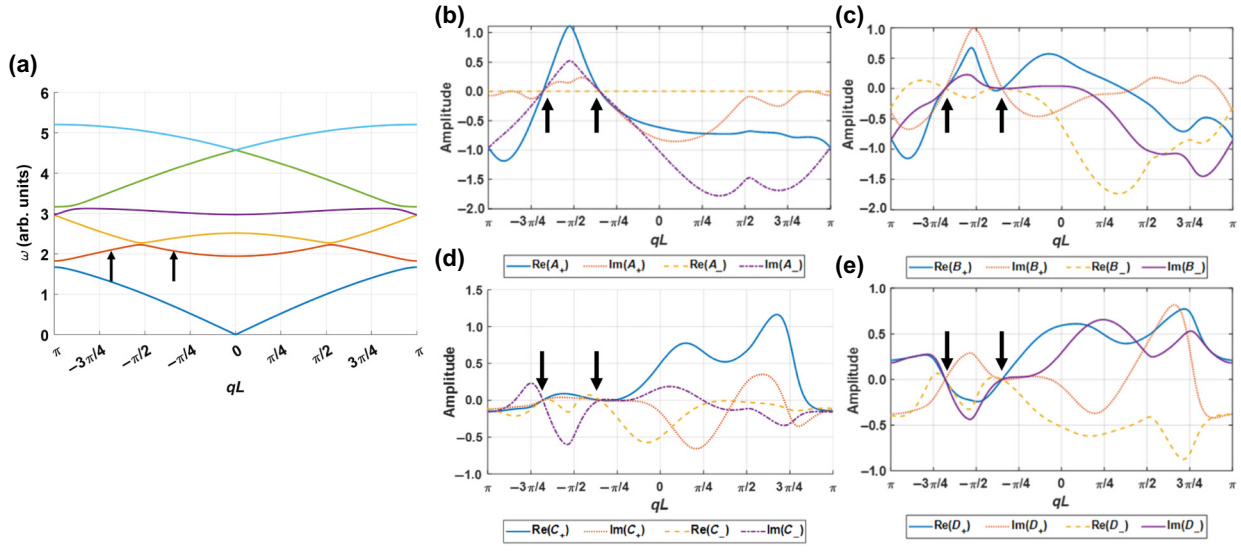

FIG. 21. (a) Band structure of the coupled system with $K_1 = (2.7/1.6)^2$, $K_2 = (2.0/1.6)^2$, $K_3 = K_4 = (4.0/1.6)^2$, and $\alpha = \alpha_1 = \alpha_2 = (2.2/1.6)^2$. The black arrows show the zeros in amplitudes. (b)–(e). Amplitudes of the masses for the second band of the coupled system, which is representative of the 5/10 SL deposited on the LN substrate.

To determine the amplitudes, the conditions of continuity of force and continuity of displacement at interfaces I and II are applied. After algebraic manipulation, we obtain eight equations that can be written in the following matrix form:

$$\begin{pmatrix} \alpha - K_1\delta_-^1 & \alpha - K_1\delta_+^1 & K_2 e^{-iqL}\alpha_2\delta_-^2 & K_2\beta_2 e^{-iqL}\delta_+^2 & -\alpha & -\alpha & 0 & 0 \\ K_1\alpha_1\delta_-^1 & K_1\beta_1\delta_+^1 & \alpha - K_2\delta_-^2 & \alpha - K_2\delta_+^2 & 0 & 0 & -\alpha & -\alpha - \alpha \\ \alpha_1 & \beta_1 & -1 & -1 & 0 & 0 & 0 & 0 \\ 1 & 1 & -e^{iQL}\alpha_2 & -e^{iQL}\beta_2 & 0 & 0 & 0 & 0 \\ 0 & 0 & 0 & 0 & 1 & 1 & -e^{-iqL}\alpha_2 & -e^{-iqL}\beta_2 \\ 0 & 0 & 0 & 0 & \alpha_1 & \beta_1 & -1 & -1 \\ -\alpha & -\alpha & 0 & 0 & \alpha - K_3\delta_-^1 & \alpha - K_3\delta_+^1 & K_4 e^{-iqL}\alpha_2\delta_-^2 & K_4 e^{-iqL}\beta_2\delta_+^2 \\ 0 & 0 & -\alpha & -\alpha & K_3\alpha_1\delta_-^1 & K_3\beta_1\delta_+^1 & \alpha - K_4\delta_-^2 & \alpha - K_4\delta_+^2 \end{pmatrix} \begin{pmatrix} A_+ \\ A_- \\ B_+ \\ B_- \\ C_+ \\ C_- \\ D_+ \\ D_- \end{pmatrix} = 0, \tag{D4}$$

where $\alpha_1 = \frac{1}{\beta_1} = e^{ik_1 a} = e^{ik_1 d_1}$, $\alpha_2 = \frac{1}{\beta_2} = e^{ik_2 2a} = e^{ik_2 d_2}$, and $\delta_\pm^{(j)} = 1 - e^{\pm ik_j a}$.

It may be noted that by our making $\alpha = 0$, the above matrix becomes a system of two uncoupled mass-spring chains, (namely, K1-K2-K2 and K3-K4-K4). In the case of the K1-K2-K2 mass-spring chain, the system of the four equations was solved numerically by the singular value decomposition method. To reveal the unconventional topological behavior of the K1-K2-K2 subsystem, we applied a gauge transformation by rescaling all numerical components, A_+, A_-, B_+, B_-. In Fig. 20 we plot the real and imaginary amplitudes of A_+ and A_- in the second band of the band structure. The behavior matches the known analytical solutions for this subsystem [51–53,69]. Figure 20 clearly shows a DRAK mode in the second band. This mode has zero amplitudes A_+, A_-, B_+, B_- on the left side of the Brillouin zone and nonzero amplitudes on the right side. This feature is associated with a Berry phase of π for that band and therefore reflects the nonconventional topology of that band. The DRAK mode emerges due to FP resonance in the second segment of the UC when the condition $\sin k_2 d_2 = 0$ is satisfied.

We now consider the case $\alpha \neq 0$—that is, the coupled system. We solve Eq. (D4) in the same way as in the case of the uncoupled system. We apply the same gauge transformation as in that case. The amplitudes of the masses are

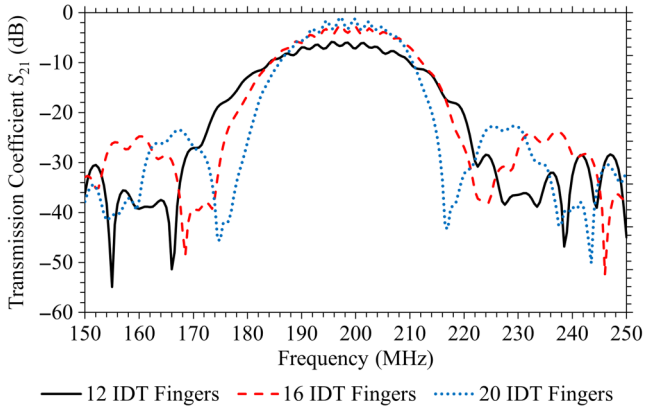

FIG. 22. Effect of increasing the number of IDT fingers on the bandwidth and transmission level of the SAW propagating through the delay line with a free surface. Increasing the number of IDT fingers decreases the bandwidth and increases the transmission level of the propagated signal.

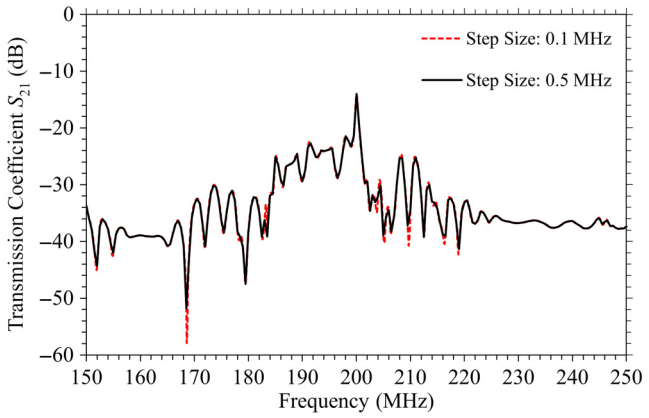

FIG. 23. Convergence of the FEA solution for the frequency increment. A step size of 0.5 MHz results in convergence of the FEA solution.

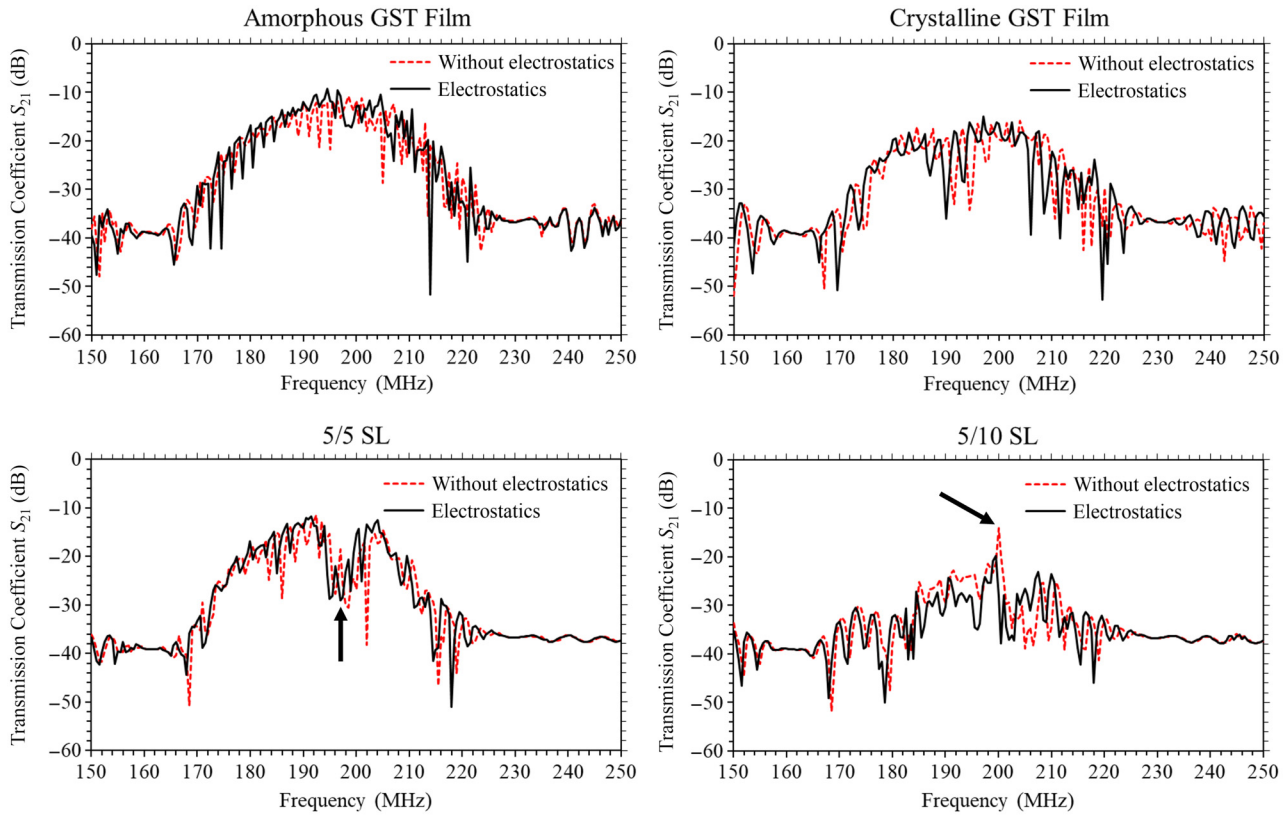

FIG. 24. Transmission spectra of SAW devices with and without consideration of the dielectric properties of the amorphous and crystalline GST materials. The arrows in the 5/5 SL and 5/10 SL plots indicate the stop band and the DRAK mode, respectively.

plotted for the second band of the coupled system in Figs. 21(b)–21(e). The graphs reveal striking asymmetry in the amplitudes across the Brillouin zone that is reminiscent of the K1-K2-K2 system. The zero amplitudes [black arrows in the band structure shown in Fig. 21(a)] in the negative region of qL show the existence of the FP resonance, which is associated with DRAK modes, providing evidence for the nonconventional topology of the second band.

APPENDIX E: EFFECT OF THE NUMBER OF IDT FINGERS ON THE FREQUENCY RESPONSE

A numerical study was performed to investigate the effect of the number of fingers in the IDTs, and revealed that increasing the number of fingers decreases the bandwidth and increases the intensity of the propagating SAW, as shown in Fig. 22.

APPENDIX F: CONVERGENCE OF THE SOLUTION FOR FREQUENCY STEP SIZE

The convergence test plays a crucial role in assessment of the accuracy of results and for the optimization of computational resources in numerical studies. The result of the convergence study is shown in Fig. 23.

APPENDIX G: TRANSMISSION SPECTRUM AFTER CONSIDERATION OF THE DIELECTRIC PROPERTIES IN FILMS AND SUPERLATTICES

We conducted a series of calculations to account for the effect of the dielectric properties of the crystalline and amorphous materials on the transmission response of SAW devices with homogeneous crystalline and amorphous films as well as 5/5 and 5/10 SLs; the corresponding responses are shown in Fig. 24. The results show that while the dielectric properties quantitatively affect the transmission, the overall qualitative behavior of the bandgap and the DRAK mode observed in the case of the 5/5 and 5/10 SLs is retained.

[1] D. P. Morgan, Surface acoustic wave devices and applications. Introductory review, Ultrasonics **11**, 211 (1973).

[2] R. F. Mitchell, Surface acoustic wave devices and applications. 4. Bandpass filters, Ultrasonics **12**, 29 (1974).

[3] P. Zhang, H. Wang, F. Zhang, S. Zhang, and G. Cao, A spurious-free SAW filter employing a novel transducer structure on bulk $LiNbO_3$ substrates, Sens. Actuators, A **379**, 115940 (2024).

[4] P. Chen, G. Li, and Z. Zhu, Development and application of SAW filter, Micromachines **13**, 656 (2022).

[5] P. V. Wright, in *Proceedings—IEEE Ultrasonics Symposium* (1992), pp. 29.

[6] C. K. Kent, N. Ramakrishnan, and H. Pratama Kesuma, Advancements in one-port surface acoustic wave (SAW) resonators for sensing applications: A review, IEEE Sens. J. **24**, 17337 (2024).

[7] W. Geng, Caiqin Zhao, Feng Xue, Xiaojun Qiao, Jinlong He, Gang Xue, Yukai Liu, Huifen Wei, Kaixi Bi, Linyu Mei, and Xiujian Chou, Influence of structural parameters on performance of SAW resonators based on 128° YX $LiNbO_3$ single crystal, Nanomaterials **12**, 2109 (2022).

[8] Y. Liu, H. Wang, F. Zhang, L. Gou, S. Zhang, G. Cao, and P. Zhang, High-performance SAW resonator with spurious modes suppression using hexagonal weighted electrode structure, Sensors **23**, 9895 (2023).

[9] B. Hu, S. Zhang, H. Zhang, W. Lv, C. Zhang, X. Lv, and H. San, Fabrications of L-band $LiNbO_3$-based SAW resonators for aerospace applications, Micromachines **10**, 349 (2019).

[10] Y. Xu, W. Fu, C.-L. Zou, Z. Shen, and H. X. Tang, High quality factor surface Fabry–Perot cavity of acoustic waves, Appl. Phys. Lett. **112**, 073505 (2018).

[11] C. Liang, C. Yan, S. Zhai, Y. Wang, A. Hu, W. Wang, and Y. Pan, Recent progress in flexible surface acoustic wave sensing technologies, Micromachines **15**, 357 (2024).

[12] Y. Pan, C. Yan, X. Gao, J. Yang, T. Guo, L. Zhang, and W. Wang, A passive wireless surface acoustic wave (SAW) sensor system for detecting warfare agents based on fluoroalcohol polysiloxane film, Microsyst. Nanoeng. **10**, 1 (2024).

[13] B. Cui, W. Wang, L. Cheng, J. Jin, A. Hu, Z. Ren, X. Xue, and Y. Liang, Acoustic impedance-based surface acoustic wave chip for gas leak detection and respiratory monitoring, Commun. Eng. **4**, 1 (2025).

[14] D. Mandal and S. Banerjee, Surface acoustic wave (SAW) sensors: Physics, materials, and applications, Sensors **22** (3), 820 (2022).

[15] M. Z. Aslam, H. Zhang, V. S. Sreejith, M. Naghdi, and S. Ju, Advances in the surface acoustic wave sensors for industrial applications: Potentials, challenges, and future directions: A review, Measurement: J. Int. Meas. Confed. **222**, 113657 (2023).

[16] C. H. Tsai, T. H. Hsu, Z. Q. Lee, C. C. Lin, Y. C. Yu, S. S. Tung, and M. H. Li, in *IEEE International Ultrasonics Symposium, IUS* (2023), pp. 1.

[17] A. Coon, in *Proceedings—IEEE Ultrasonics Symposium* (1991), pp. 155.

[18] A. A. Maradudin and G. I. Stegeman, *Surface Acoustic Waves* (Springer-Verlag, Berlin, Heidelberg, 1991).

[19] R. M. White and F. W. Voltmer, Direct piezoelectric coupling to surface elastic waves, Appl. Phys. Lett. **7**, 314 (1965).

[20] A. S. Koigerov, Modern physical-mathematical models and methods for design surface acoustic wave devices: COM based P-matrices and FEM in COMSOL, Mathematics **10**, 4353 (2022).

[21] V. Yantchev, V. Plessky, and I. Katardjiev, Fundamentals of the grating-assisted surface acoustic wave-plate bulk acoustic wave interaction, J. Appl. Phys. **104**, 034111 (2008).

[22] C. Cai, Y. Xu, L. Gao, S. Deng, and D. Wu, Surface wave isolation by variable depth infilled trenches, Sci. Total Environ. **953**, 176071 (2024).

[23] N. E. Glass, R. Loudon, and A. A. Maradudin, Propagation of Rayleigh surface waves across a large-amplitude grating, Phys. Rev. B **24**, 6843 (1981).

[24] N. E. Glass and A. A. Maradudin, Leaky surface-elastic waves on both flat and strongly corrugated surfaces for isotropic, nondissipative media, J. Appl. Phys. **54**, 796 (1983).

[25] Y. Yang, C. Dejous, and H. Hallil, Trends and applications of surface and bulk acoustic wave devices: A review, Micromachines **14**, 43 (2023).

[26] P. E. Timoshenko, V. V. Kalinchuk, and V. B. Shirokov, Finite-element analysis of scattering parameters of surface acoustic wave bandpass filter formed on barium titanate thin film, Int. J. Smart Nano Mater. **9**, 88 (2018).

[27] T. Zhou, A. Reinhardt, M. Bousquet, J. Eymery, S. Leake, M. V. Holt, P. G. Evans, and T. Schülli, High-resolution high-throughput spatio-temporal strain imaging reveals loss mechanisms in a surface acoustic wave device, Nat. Commun. **16**, 2822 (2025).

[28] J. Zhang, B. Hu, and S. Wang, Review and perspective on acoustic metamaterials: From fundamentals to applications, Appl. Phys. Lett. **123**, 010502 (2023).

[29] E. Yablonovitch, Photonic Crystals, J. Mod. Opt. **41**, 173 (1994).

[30] E. Yablonovitch, Inhibited spontaneous emission in solid-state physics and electronics, Phys. Rev. Lett. **58**, 2059 (1987).

[31] M. S. Kushwaha, P. Halevi, L. Dobrzynski, and B. Djafari-Rouhani, Acoustic band structure of periodic elastic composites, Phys. Rev. Lett. **71**, 2022 (1993).

[32] M. M. Sigalas and E. N. Economou, Comment on "Acoustic band structure of periodic elastic composites,", Phys. Rev. Lett. **75**, 3580 (1995).

[33] T.-T. Wu, J.-C. Hsu, J.-H. Sun, and S. Benchabane, in *Phononic Crystals: Fundamentals and Applications*, edited by A. Khelif, and A. Adibi (Springer, New York, 2016), pp. 145–189.

[34] J. Liu, H. Guo, and T. Wang, A review of acoustic metamaterials and photonic crystals, Crystals **10**, 1 (2020).

[35] B. Zhang, Topological acoustics unlocks new horizons in microfluidics: Acoustic metamaterials, Nat. Mater. **24**, 652 (2025).

[36] S. Benchabane, A. Khelif, J.-Y. Rauch, L. Robert, and V. Laude, Evidence for complete surface wave band gap in a piezoelectric phononic crystal, Phys. Rev. E **73**, 065601 (2006).

[37] S. Benchabane, A. Khelif, A. Choujaa, B. Djafari-Rouhani, and V. Laude, Interaction of waveguide and localized modes in a phononic crystal, Europhys. Lett. **71**, 570 (2005).

[38] Y. Achaoui, V. Laude, S. Benchabane, and A. Khelif, Local resonances in phononic crystals and in random arrangements of pillars on a surface, J. Appl. Phys. **114**, 104503 (2013).

[39] Y. Achaoui, A. Khelif, S. Benchabane, L. Robert, and V. Laude, Experimental observation of locally-resonant and Bragg band gaps for surface guided waves in a phononic crystal of pillars, Phys. Rev. B **83**, 1 (2011).
[40] B. J. Ash, S. R. Worsfold, P. Vukusic, and G. R. Nash, A highly attenuating and frequency tailorable annular hole phononic crystal for surface acoustic waves, Nat. Commun. **8**, 1 (2017).
[41] M. Oudich, N. J. R. K. Gerard, Y. Deng, and Y. Jing, Tailoring structure-borne sound through bandgap engineering in phononic crystals and metamaterials: A comprehensive review, Adv. Funct. Mater. **33**, 35 (2023).
[42] H. Xue, Y. Yang, and B. Zhang, Topological acoustics, Nat. Rev. Mater. **7**, 974 (2022).
[43] X. Zhang, F. Zangeneh-Nejad, Z.-G. Chen, M. H. Lu, and J. Christensen, A second wave of topological phenomena in photonics and acoustics, Nature **618**, 687 (2023).
[44] A. Alù, C. Daraio, P. Deymier, and M. Ruzzene, A bright future for topological acoustics, Nat. Commun. **16**, 2 (2025).
[45] A. Alù, C. Daraio, P. A. Deymier, and M. Ruzzene, Topological acoustics, Acoust. Soc. Am. **13**, 13 (2021).
[46] P. A. Deymier, J. O. Vasseur, K. Runge, A. Khanikaev, and A. Alù, Immunity to backscattering of bulk waves in topological acoustic superlattices, Crystals **14**, 344 (2024).
[47] N. Swinteck, S. Matsuo, K. Runge, J. O. Vasseur, P. Lucas, and P. A. Deymier, Bulk elastic waves with unidirectional backscattering-immune topological states in a time-dependent superlattice, J. Appl. Phys. **118**, 063103 (2015).
[48] L. M. Nash, D. Kleckner, A. Read, V. Vitelli, A. M. Turner, and W. T. M. Irvine, Topological mechanics of gyroscopic metamaterials, Proc. Natl. Acad. Sci. U. S. A. **112**, 14495 (2015).
[49] R. Fleury, D. L. Sounas, C. F. Sieck, M. R. Haberman, and A. Alù, Sound isolation and giant linear nonreciprocity in a compact acoustic circulator, Science **343**, 516 (2014).
[50] A. B. Khanikaev, R. Fleury, S. H. Mousavi, and A. Alù, Topologically robust sound propagation in an angular-momentum-biased graphene-like resonator lattice, Nat. Commun. **6**, 1 (2015).
[51] P. A. Deymier, K. Runge, and J. O. Vasseur, Geometric phase and topology of elastic oscillations and vibrations in model systems: Harmonic oscillator and superlattice, AIP Adv. **6**, 121801 (2016).
[52] P. A. Deymier and K. Runge, One-way propagation of topologically non-conventional bulk transverse elastic waves in infinite and finite superlattices: Application to low-loss acoustic wave devices, Appl. Phys. Lett. **123**, 012202 (2023).
[53] M. Xiao, Z. Q. Zhang, and C. T. Chan, Surface impedance and bulk band geometric phases in one-dimensional systems, Phys. Rev. X **4**, 1 (2014).
[54] M. Wuttig and N. Yamada, Phase-change materials for rewriteable data storage, Nat. Mater. **6**, 824 (2007).
[55] M. Wuttig, H. Bhaskaran, and T. Taubner, Phase-change materials for non-volatile photonic applications, Nat. Photonics **11**, 465 (2017).
[56] J. Pries, S. Wei, M. Wuttig, and P. Lucas, Switching between crystallization from the glassy and the undercooled liquid phase in phase change material $Ge_2Sb_2Te_5$, Adv. Mater. **31**, 1900784 (2019).
[57] S. R. Nandakumar, M. Le Gallo, I. Boybat, B. Rajendran, A. Sebastian, and E. Eleftheriou, A phase-change memory model for neuromorphic computing, J. Appl. Phys. **124**, 152135 (2018).
[58] H. Nazeer, H. Bhaskaran, L. A. Woldering, and L. Abelmann, Young's modulus and residual stress of GeSbTe phase-change thin films, Thin Solid Films **592**, 69 (2015).
[59] I.-M. Park, J.-K. Jung, S.-O. Ryu, K.-J. Choi, B.-G. Yu, Y.-B. Park, S. M. Han, and Y.-C. Joo, Thermomechanical properties and mechanical stresses of $Ge_2Sb_2Te_5$ films in phase-change random access memory, Thin Solid Films **517**, 848 (2008).
[60] M. J. Müller, Carmen Morell, Peter Kerres, Mohit Raghuwanshi, Ramon Pfeiffer, Sebastian Meyer, Christian Stenz, Jiangjing Wang, Dmitry N. Chigrin, Pierre Lucas, and Matthias Wuttig, Decoupling nucleation and growth in fast crystallization of phase change materials, Adv. Funct. Mater. **34**, 1 (2024).
[61] G. W. Burr, P. Tchoulfian, T. Topuria, C. Nyffeler, K. Virwani, A. Padilla, R. M. Shelby, M. Eskandari, B. Jackson, and B.-S. Lee, Observation and modeling of polycrystalline grain formation in $Ge_2Sb_2Te_5$, J. Appl. Phys. **111**, 0 (2012).
[62] M. M. Elsherbini, M. F. Elkordy, and A. M. Gomaa, Using COMSOL to model high frequency surface acoustic wave (SAW) device, Mater. Eng. **8**, 1 (2016).
[63] A. S. Koigerov and A. V. Korlyakov, Finite element modeling of surface acoustic wave devices using COMSOL, Russ. Microelectron. **51**, 226 (2022).
[64] Q. Zhang, Z. Chen, Y. Chen, J. Dong, P. Tang, S. Fu, H. Wu, J. Ma, and X. Zhao, Periodic analysis of surface acoustic wave resonator with dimensionally reduced PDE model using COMSOL code, Micromachines **12**, 1 (2021).
[65] R. D. Janardhana and N. Jackson, A simulated investigation of lithium niobate orientation effects on standing acoustic waves, Sensors **23**, 8317 (2023).
[66] R. Lu, Y. Yang, S. Link, and S. Gong, A1 Resonators in 128 Y-cut lithium niobate with electromechanical coupling of 46.4%, J. Microelectromech. Syst. **29**, 313 (2020).
[67] David Morgan, *Surface Acoustics Wave Filters* (Elsevier, Amsterdam, 2007), Vol. 91.
[68] K. Hashimoto, *Surface Acoustic Wave Devices in Telecommunications* (Springer-Verlag, Berlin, 2000).
[69] P. A. Deymier, K. Runge, A. Khanikaev, and A. Alù, Pseudo-spin polarized one-way elastic wave eigenstates in one-dimensional phononic superlattices, Crystals **14**, 1 (2024).
[70] Y. Roh and S. Lee, Development of a SAW duplexer with one-chip isolation circuits, Ultrasonics **42**, 413 (2004).
[71] J. Tao, Z. Tang, Y. Zou, B. Wang, J. Li, Y. Liu, and T. Wu, A phase canceling technique to improve SAW duplexer isolation, Micromachines **14**, 239 (2023).
[72] A. A. Maradudin, in *Physics of Phonons*, edited Gerhard Ertl (Springer Nature, Karpacz, Poland, 1987), pp. 82–147.
[73] L. Shao, Smarak Maity, Lu Zheng, Lue Wu, Amirhassan Shams-Ansari, Young-Ik Sohn, Eric Puma, M. N. Gadalla, Mian Zhang, Cheng Wang, Evelyn Hu, Keji Lai, and Marko Lončar, Phononic band structure engineering for high-Q

gigahertz surface acoustic wave resonators on lithium niobate, Phys. Rev. Appl. **12**, 014022 (2019).

[74] Q. Wang, E. T. F. Rogers, B. Gholipour, C.-M. Wang, G. Yuan, J. Teng, and N. I. Zheludev, Optically reconfigurable metasurfaces and photonic devices based on phase change materials, Nat. Photonics **10**, 60 (2016).

[75] J. Zheng, Zhuoran Fang, Changming Wu, Shifeng Zhu, Peipeng Xu, Jonathan K. Doylend, Sanchit Deshmukh, Eric Pop, Scott Dunham, and Arka Majumdar, Nonvolatile electrically reconfigurable integrated photonic switch enabled by a silicon PIN diode heater, Adv. Mater. **32**, 1 (2020).

[76] Z. Fang, Rui Chen, Jiajiu Zheng, Asir Intisar Khan, Kathryn M. Neilson, Sarah J. Geiger, Dennis M. Callahan, Michael G. Moebius, Abhi Saxena, Michelle E. Chen, Carlos Rios, Juejun Hu, Eric Pop, and Arka Majumdar, Ultra-low-energy programmable non-volatile silicon photonics based on phase-change materials with graphene heaters, Nat. Nanotechnol. **17**, 842 (2022).